Materials & Design 217 (2022) 110593

Contents lists available at ScienceDirect

Materials & Design

journal homepage: www.elsevier.com/locate/matdes

The $AlMo_{0.5}NbTa_{0.5}TiZr$ refractory high entropy superalloy: Experimental findings and comparison with calculations using the CALPHAD method

Patricia Suárez Ocaño [a,*], Suzana G. Fries [b], Inmaculada Lopez-Galilea [c], Reza Darvishi Kamachali [a], Janina Roik [d], Leonardo Agudo Jácome [a]

[a] Federal Institute for Materials Research and Testing (BAM), Department for Materials Engineering, Unter den Eichen 87, 12205 Berlin, Germany
[b] Materials Research Department (MRD), Ruhr-University Bochum, Universitätsstr. 150, 44801 Bochum, Germany
[c] Institute for Materials, Ruhr-University Bochum, Universitätsstr. 150, 44801 Bochum, Germany
[d] Federal Institute for Materials Research and Testing (BAM), Department of Inorganic Reference Materials, Richard-Willstätter-Strasse 11, 12489 Berlin-Adlershof, Germany

HIGHLIGHTS

- Microstructural characterization of the $AlMo_{0.5}NbTa_{0.5}TiZr$ refractory superalloy in the as-cast state is reported for the first time and compared with hitherto known annealed state.
- The detailed CALPHAD analysis with Scheil-Gulliver and equilibrium calculations reveal new insights into understanding the nature of the studied alloy by comparing with the experimental data.
- The equilibrium-based CALPHAD approach used here pinpoints the presence of a miscibility gap between two bcc-based phases, confirming the hypothesis that this alloy is formed by spinodal decomposition.
- Differential thermal analysis was reported for the first time for this alloy, revealing a good agreement between measured phase transformation temperatures and calculated values.

GRAPHICAL ABSTRACT

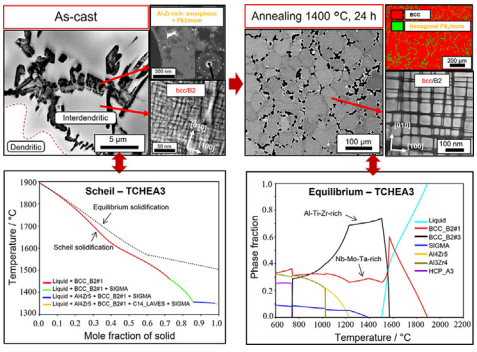

ARTICLE INFO

Article history:
Received 28 January 2022
Revised 23 March 2022
Accepted 23 March 2022
Available online 26 March 2022

Keywords:
CALPHAD database analysis

ABSTRACT

Detailed microstructural characterization of the $AlMo_{0.5}NbTa_{0.5}TiZr$ refractory high entropy superalloy in the as-cast state is reported for first time and compared with the state annealed at 1400 °C for 24 h. The former shows a dendritic structure, with a mixture of A2/B2 phases < 20 nm in both the dendritic and interdendritic regions. A mostly amorphous phase, rich in Al and Zr, is found within the interdendritic region. The annealed state reproduced the combination of A2/B2/Al-Zr-rich phases reported previously. Calculations from two relevant ThermoCalc databases were compared with the experimental results. Equilibrium calculations were compared with results for the annealed alloy, whereas solidification paths calculated using Scheil-Gulliver model were used for comparison with the as-cast alloy. A previously

* Corresponding author.
E-mail address: patricia.suarez-ocano@bam.de (P. Suárez Ocaño).

https://doi.org/10.1016/j.matdes.2022.110593

Refractory superalloys
Chemically complex alloy
Characterization
Microstructure.

hypothesized spinodal decomposition during cooling as the mechanism responsible for the patterned A2/B2 microstructure is confirmed via the CALPHAD calculations, pointing to its use as an efficient design tool for such alloys. Finally, the comparison between the experimental and computational findings allowed better understanding the solidification path and equilibrium stability of this alloy, giving a base to make better decisions on the field of new refractory superalloy design.

1. Introduction

To improve the performance of future structural components for high temperature applications, it is necessary to develop new materials that can withstand higher temperatures than at present while retaining high strength and good creep and corrosion resistance. Ni-base superalloys have been in the last decades the material of choice for severe service conditions [1–4]. The realm of chemically complex alloys (CCAs), materials that lack a base element but instead are composed of several of them at high compositions, has been increasingly studied in the last years thanks to their interesting and sometimes unexpected microstructures and properties. The CCAs made of refractory elements such as Mo, Nb and Ta are attractive candidates for use at extremely high temperatures (associated with many technological applications) [5–7]. An example of a refractory CCAs is the $AlMo_{0.5}NbTa_{0.5}TiZr$, which has a measured density of 7.4 g/cm^3, Vickers microhardness (Hv of 5.8 ± 0.1 GPa = 591.4 HV1) and a high temperature (compressive) strength of 772 MPa at 1000 °C with a fracture strain < 50% [8,9]. One drawback of this alloy is its room temperature ductility of δ = 10% [8]. Senkov et al. [8] and Jensen et al. [10] reported that a coherent two-phase nanostructure forms for the $AlMo_{0.5}NbTa_{0.5}$-TiZr alloy after applying a heat treatment under argon atmosphere. The obtained microstructure resembles the γ/γ pattern of the Ni-base superalloys, $L1_2$ cuboids (γ) embedded in a continuous fcc matrix (γ) [4], therefore naming it *refractory high entropy superalloy* (RSA) [8–11]. This resemblance promotes the possibility of profiting from the long-term knowledge gained on the effectiveness of such microstructures to high temperature performance. However, important differences exist, e.g.: 1) the dimensions of the cuboid/-matrix structure are one order of magnitude smaller; 2) the nanostructure is formed by cuboidal A2 phase (discontinuous) particles embedded in a continuous B2 phase matrix, i.e. the matrix is made of an ordered phase, opposite to Ni-base superalloys; and 3) there is a strong partitioning of Mo, Nb and Ta to the A2 phase, and of Al, Ti and Zr to the B2 phase [8,10].

Beyond the high strength at high temperatures, and the presence of refractory elements, the $AlMo_{0.5}NbTa_{0.5}TiZr$ RSA contains ≈ 20% of Al (to lower its density) that has been determined to form an intermetallic rich in Al and Zr, but also significantly lowers its melting point. However, there is no clear study in the literature indicating whether this RSA has a higher melting point than Ni-based alloys or not. In the case of having a higher melting point, this alloy could be attractive for use at extremely high temperatures, and therefore, this is also addressed in this contribution. As CCAs contain multiple principal elements, which contrasts with conventional alloys, it has been challenging to understand the phase equilibrium and solidification path of alloys like the RSA. In recent years, CALPHAD-based methodologies have been used largely in the field of CCAs to understand their formation and to their optimization [12–15]. Senkov et al. [16] calculated the equilibrium and non-equilibrium diagrams using the Pandat Ti database and showed the formation of two phases, BCC and Al_2Zr_3, after non-equilibrium solidification and three phases, BCC, Ti_3Al and Al_2Zr_3, in equilibrium. A clear mismatch however was found between these results and their experimental measurements [16] while the phases formed during casting have not been assessed, e.g., by comparing the as-cast state and the non-equilibrium calculations. Nevertheless, considering the importance of the initial solidification process of refractory alloys with respect to the ability to effectively tune their properties by subsequent heat treatments, a step back to understand the casting behavior of this RSA can shed insights into improving it. Whitfield et al. [17] calculated the phase equilibria using the SSol5 database, which demonstrated better agreement to the phases observed experimentally, although large differences were found in the solvus temperatures, especially for the Al_4Zr_5 intermetallic phase. Thus, it seems like the simple use of available databases for CALPHAD calculations of such multi-principal elements is not enough to establish robust phase stability anticipations for this alloy system and presumably its derivates. Here the use of analytical and of structural characterization methods is still much needed in the field of CCAs [18] to further aid the development and validation of the developing CALPHAD databases.

In the present work, we aim to understand the phase stability and solidification behavior of the RSA $AlMo_{0.5}NbTa_{0.5}TiZr$ as a base to tackle similar systems. To this end, an approach was implemented where detailed CALPHAD thermodynamic stabilities and solidification paths were calculated and compared with experimental data found for both as-cast, AC, and annealed state, AN (AC + 1400 °C for 24 h). The processing of most HEAs is still based on trial and error. In this context, the study of the as-cast structures needs special attention, to allow better design of heat treatments that may help to overcome the room-temperature embrittlement in this and similar high-temperature alloys or to pinpoint detrimental microstructural features that may not be reverted by heat treatment. In addition, a comparison with CALPHAD Scheil solidification is used to benchmark two published databases and to assist future CALPHAD-integrated RSA design. Furthermore, the results go beyond the state-of-the-art [8,10,17] by directly comparing CALPHAD equilibrium calculations and differential thermal analysis in the annealed state, casting light on the phase transformation pathways and temperatures. The experimental data are accompanied with CALPHAD calculations that were conducted using the commercial thermodynamic software ThermoCalc [19] with two different databases, the established TCNI10 and TCHEA3, in order to evaluate the accuracy for this alloy. The database TCHEA4 was used for all the calculations as well; however, only the results obtained with the TCHEA3 are reported since this shows a better match with the experimental data. The current experimental and computational findings assist the better design of refractory high-entropy alloys.

2. Material and methods

2.1. Material (as-cast and heat treated)

The $AlMo_{0.5}NbTa_{0.5}TiZr$ alloy was prepared by vacuum arc melting of the pure elements in an argon atmosphere (purity > 99.998%, with small impurities of H_2O (<5 v-ppm), O_2 (<5 v-ppm) and N_2 (<10 v-ppm), following the description given by Senkov et al. [16] but with some differences. Aluminum was in the form of granules (2–10 mm) with a purity of 99.99%, molybdenum in the form

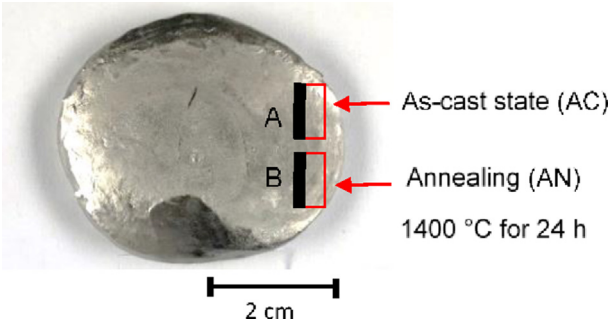

Fig. 1. Sample (button) obtained by vacuum arc melting which shows from where the casting and annealed samples were obtained for subsequent characterization. The surfaces marked as "A" and "B", show the region where the SEM and TEM analysis were performed in the AC and AN, respectively, with the analyzed surfaces being on the black rectangular regions and orthogonal to the plane of the image.

of 0.5 mm thick sheet with a purity of 99.99% and niobium was in form of granules ranging 2–10 mm with 99.9% of purity. Tantalum was in the form of pellets of 6 × 6 mm, titanium in the form of pieces < 5 mm and zirconium in the form of granules (1–3 mm) and their purities were 99.9%, 99.5%, 99.9%, respectively. Arc melting was conducted on a water-cooled copper plate. High-purity molten titanium was used as a getter for residual oxygen, nitrogen, and hydrogen. To achieve a homogeneous distribution of elements in the alloy, the button was re-melted seven times, flipped for each melt, and kept in a liquid state for ≈ 5 min during each melting event. After casting, the sample was cut as is shown in Fig. 1 to get the as-cast sample for characterization. Another piece of sample was cut from the button, as shown in Fig. 1, and was annealed at 1400 °C for 24 h in continuously flowing high-purity argon to homogenize the grain structure, and cooled at a cooling rate after annealing < 4 K/min.

2.2. Characterization

The alloy composition was determined by inductively coupled plasma atomic emission spectroscopy (ICP-OES) and is given in Table 1.

Differential Thermal Analysis (DTA, SETERAM TAG24), was used to determine the main temperature transformations. Measurements were conducted by placing a small specimen of ≈ 20 mg in an open corundum crucible at a heating rate of 5 K/min up to a maximum temperature of 1620 °C (limit of the DTA facility). Cooling to room temperature was carried out at –5 K/min. For signal correction, a measurement of an empty crucible was conducted with the same experimental conditions.

Bulk phase analysis was conducted by X-ray diffractometry (Seifert PTS 3000), Co Kα radiation ($\lambda_{K\alpha1}$ = 1.7902 Å) and a 2Θ scattering range of 10–100° for the as-cast state (AC), and 10 – 120° for the annealed (AN) alloy. The identification was carried out by comparing the experimental patterns with patterns simulated using PowderCell [20].

The microstructures of the AC and AN alloy were analyzed by scanning electron microscopy (SEM, FEI Quanta 3D) equipped with backscatter electron (BSE) and energy-dispersive X-ray spectroscopy (EDX, EDAX Octane Elect SDDs) detectors. The average grain size for the AN alloy was determined in accordance with ASTM E112 [21]. Also, electron backscattered diffraction (EBSD, SEM LEO Gemini 1530 V P Zeiss, EBSD detector Bruker e-flash HD with Bruker Esprit 1.9 EBSD-Software package) was conducted on the AN alloy at a medium magnification to determine the polycrystallinity of the A2/B2 grains and to characterize the phases forming at grain boundaries. For transmission electron microscopy (TEM), samples were cut in slices ≈ 500 μm in thickness, after which thin foils with 3 mm in diameter were prepared by mechanical polishing to ≈ 100 μm and finally thinned by twin-jet electropolishing (Struers Tenupol-3) in an electrolyte consisting of 950 mL ethanol (86.4%), 100 mL butanol (9.1%) and 50 mL perchloric acid (4.5%) at −30 °C and 30 V. The TEM was equipped with a field emission gun (FEG) source (TEM, JEOL JEM-2200FS) working at an acceleration voltage of 200 kV. Conventional (C) TEM was conducted for acquisition of energy filtered (EF) selected area diffraction patterns (SADPs) as well as bright field (BF)/dark field (DF) micrographs. Bright field and high angle annular (HAA) DF micrographs were also acquired in the scanning (S) TEM mode, the former for diffraction contrast and the latter for atomic number contrast. The SADPs were indexed with the aid of the Java version of the electron microscopy suite (JEMS) [22]. The volume fraction of the A2/B2 phases in both states was estimated using the image analysis package ImageJ [23].

2.3. Thermodynamic calculations

CALculation of PHAse Diagram (CALPHAD) is an important thermodynamic methodology based on the minimization of the total Gibbs energy of the system with different phases for a given alloy system that enables to calculate not only the phase diagram but also different thermodynamic properties of the system [24]. The CALPHAD calculations were developed using the TCNI10 and TCHEA3 databases via ThermoCalc software. Although TCNI10 is primarily optimized for Ni-based superalloys, it does cover all the edge binaries and several ternary phase diagrams of the Al-Mo-Nb-Ta-Ti-Zr system. Scheil and equilibrium solidification were calculated for the RSA using the composition determined experimentally (cf. Table 1). The Scheil-Gulliver equation describes the solute redistribution during solidification of an alloy, if perfect mixing in the liquid and no diffusion in the solid phase is assumed [25]. All calculations were performed using the experimental chemical composition in Table 1 to compare the results with the experimental data. Note that the phases will reflect their names as they are expressed in each commercial database. Thus, body centered cubic (bcc)-based phases called "BCC_B2#1" and "BCC_B2#3" do not necessarily mean that the phase is "B2".

3. Results

3.1. Microstructural characterization

3.1.1. As-cast state (AC)

The AC alloy has a typical dendritic structure with an average grain size of 75 ± 19 μm, as is shown in Fig. 2a-b. The presence of a strong segregation can also be seen inside the grains between dendritic and interdendritic regions. Due to elemental partitioning that results in different mean atomic numbers, the dendritic regions exhibit a brighter contrast and interdendritic regions exhibit darker contrast in the BSE-SEM images. A higher magnification

Table 1
Experimental chemical composition of the $AlMo_{0.5}NbTa_{0.5}TiZr$ sample represented in mole %.

Al	Mo	Nb	Ta	Ti	Zr
21.03	10.19	20.23	6.76	20.79	21.00

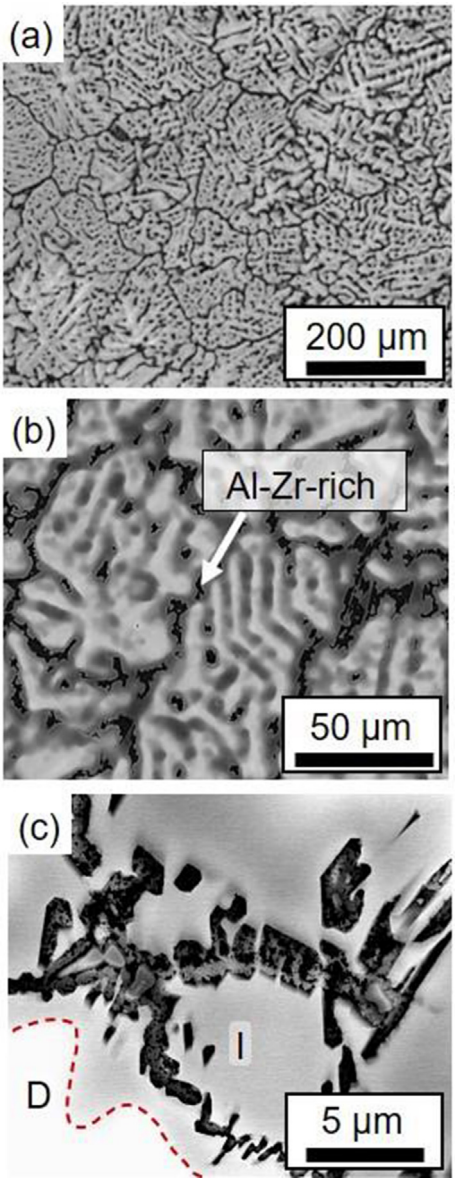

Fig. 2. SEM-BSE micrographs of the RSA in AC (a) sample center (see cut "A" in Fig. 1) (b) higher magnification showing the presence of a darker phase within the interdendritic region with the presence of an Al-Zr-rich phase (c) detail of the dark Al-Zr-rich phase acquired at a grain boundary; letters "D" and "I" respectively mark dendritic and interdendritic regions, with their diffuse boundary highlighted by a dotted red line. (For interpretation of the references to color in this figure legend, the reader is referred to the web version of this article.)

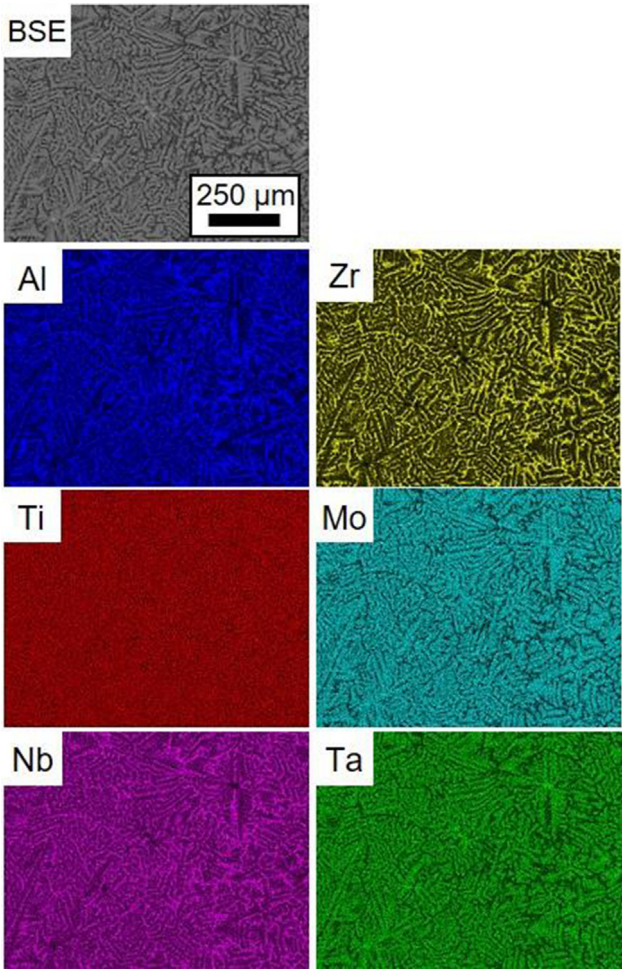

Fig. 3. EDX element mapping of components in the RSA/AC-alloy.

reveals the presence of an Al-Zr-rich network, as determined by EDX (summarized in Table 2), with the darkest contrast in the interdendritic regions (Fig. 2b-c).

Compositional maps of the alloying elements Al, Zr, Nb, Mo, Ta and Ti are shown in Fig. 3. As it can be qualitatively seen, Mo and Ta, with the highest melting points, are located preferably inside the dendritic regions, and of Al, Zr and Nb partition stronger to interdendritic regions. Ti is distributed almost evenly between dendritic and interdendritic regions, although a weak partitioning towards the latter is still visible.

In Fig. 4a-b, EBSD data is respectively presented as a pattern quality (PQ) map and inverse pole figure (IPF) from a TEM sample

Table 2
Chemical composition of the phases in the different regions in mole fraction (%) for the AC and AN alloy. The error bar is given by the standard deviation. Bold numbers show the elements of which the phase is rich.

State	Phase	Method	Region	Composition (mole fraction /%)					
				Al	**Mo**	**Nb**	**Ta**	**Ti**	**Zr**
As-cast (AC)	Al-Zr-rich	TEM-EDX	Neighboring region marked as SAD in green in Fig. 6a	**34 ± 4**	6 ± 5	9 ± 2	2 ± 1	8 ± 2	**41 ± 5**
	A2/B2	SEM-EDX	Interdendritic, e.g., "I" in Fig. 1c	**27 ± 1**	8 ± 1	17 ± 1	4 ± 1	**21 ± 1**	**23 ± 1**
	A2/B2	SEM-EDX	Dendritic, e.g., "D" in Fig. 1c	20 ± 1	**14 ± 1**	**23 ± 1**	**9 ± 1**	21 ± 1	13 ± 1
Annealed (AN)	Al-Zr-rich	TEM-EDX	Grain boundary in a similar region marked with blue row in Fig. 7b	**32 ± 2**	3 ± 1	10 ± 1	2 ± 1	7 ± 1	**47 ± 1**
	A2	TEM-EDX	Grain core (bright precipitates in Fig. A3a of supplementary data)	7 ± 1	**20 ± 1**	**35 ± 2**	**13 ± 1**	16 ± 1	9 ± 3
	B2	TEM-EDX	Grain core (dark channels in Fig. A3a of supplementary data)	**20 ± 1**	9 ± 1	19 ± 1	3 ± 1	**19 ± 1**	**30 ± 1**
	A2	SEM-EDX	Bright rim surrounding the Al-Zr-rich grain boundary in Fig. 7b	9 ± 1	**17 ± 1**	**25 ± 1**	**13 ± 1**	26 ± 1	10 ± 1

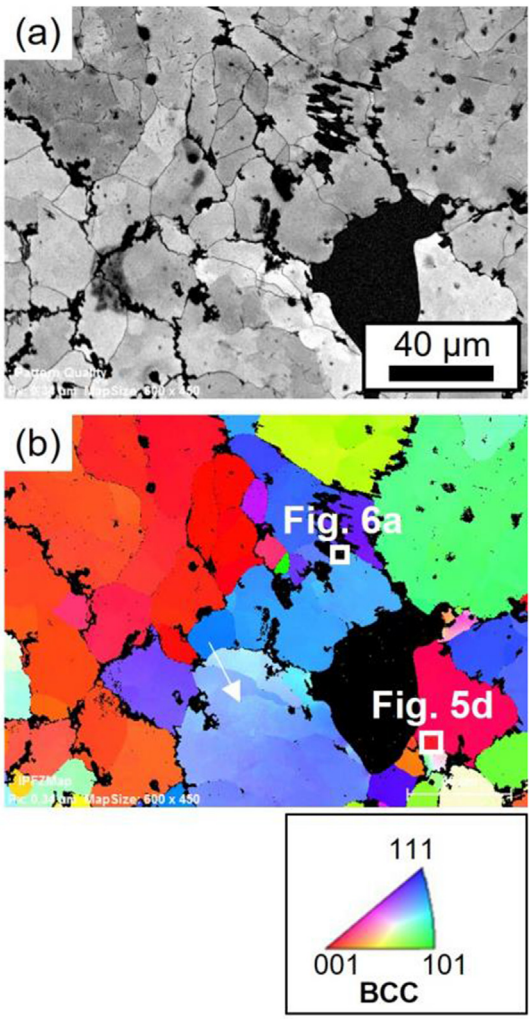

Fig. 4. EBSD maps of RSA in AC. (a) pattern quality, (b) inverse pole figure (IPFZ).

of the RSA in the AC condition (with an electron-transparent region close to large hole on lower right). The EDX-coupled EBSD system indexes the large equiaxed grains in Fig. 4 as "BCC" (Body-Centered Cubic), irrespective of location, i.e. the dendritic structure is not resolved. In turn, the IPFZ map shows subgrains separated by non-indexed regions, which have comparable sizes to secondary dendritic arms (cf. Fig. 2b). Within these subgrains, a further subdivision into smaller regions with varying orientations is seen, e.g., purplish-bluish grain bordering left side of large whole (shown by the white arrow in Fig. 4b). The grain and subgrain boundary regions rich in Al and Zr, as seen in Fig. 2, are not indexed in this map.

The nanostructure of the AC alloy was revealed by TEM. Fig. 5 shows two CTEM-DF images (a and b) and their corresponding zone axis (Z = [001]) SAD pattern (P) (c). In green, Fig. 5c shows the reflections selected to retrieve the diffraction contrasts in Fig. 5-a-b. Since the image in Fig. 5a was formed using a superlattice 100 reflection and the image in Fig. 5b was formed using a 200 reflection, the interdendritic region can be interpreted as composed of a mixture of two bcc-based phases. The insets in the bottom right of Fig. 5a-b show a magnified region marked by a white square. Three white lines in these inserts, placed at the same locations, show that different locations are illuminated in both images. Furthermore, the bright regions seem strongly interconnected in Fig. 5a. Thus,

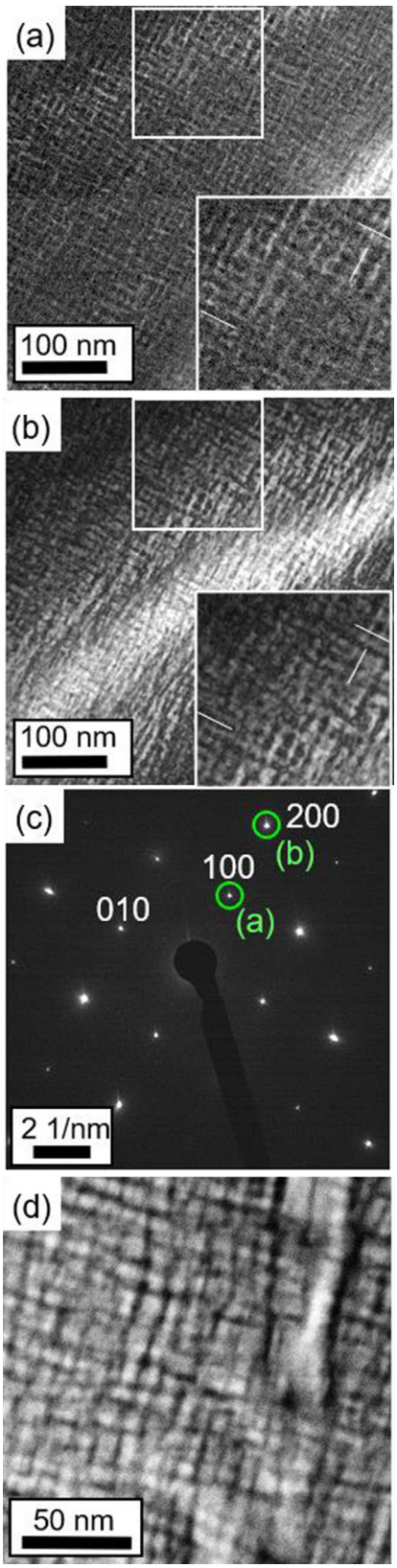

Fig. 5. (C)TEM-DF micrographs of the interdendritic zone in AC oriented along [001] zone axis: (a) using superlattice reflection (100) in (c); and (b) using reflection (200). (c) SADP with contrast apertures marked in green for images in (a) and (b). (d) STEM-HAADF micrograph of the region marked as "Fig. 5d" in the IPFZ in Fig. 4b. (For interpretation of the references to color in this figure legend, the reader is referred to the web version of this article.)

the phase with the bright contrast in Fig. 5a (matrix channels) is ordered (B2) while the remaining phase is disordered (A2). The STEM-HAADF image in Fig. 5d, acquired at a similar interdendritic location, more clearly reveals a continuous region with a low mean atomic number (dark), while discrete bright regions in between are associated to a large mean atomic number.

The Al-Zr-rich region (cf. Fig. 2b-c) was also characterized by TEM, as presented in Fig. 6. Fig. 6a shows a CTEM-BF of the Al-Zr-rich region (mostly bright areas) surrounded by thicker regions

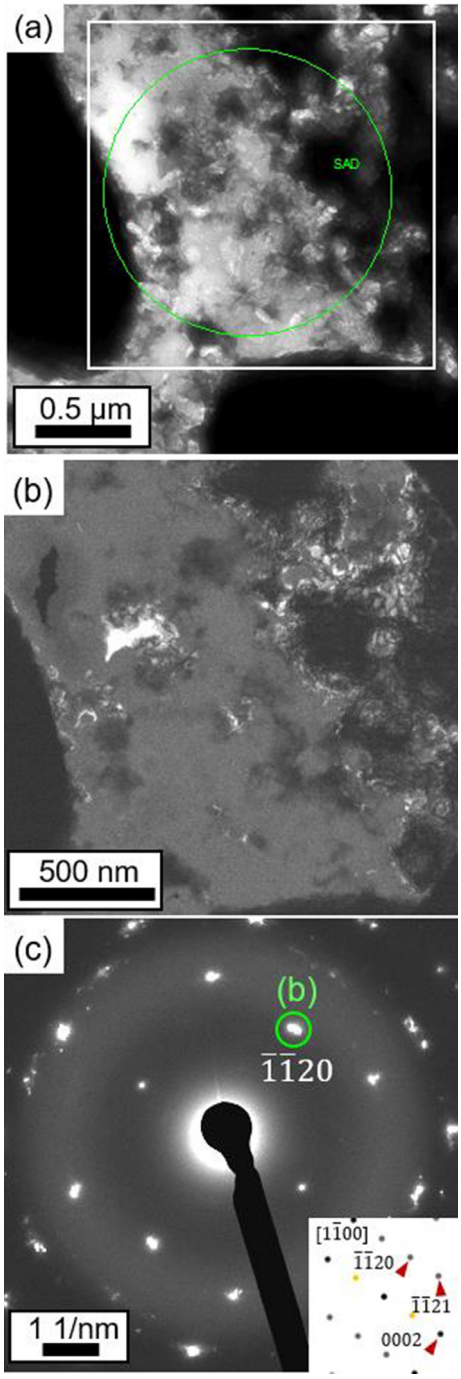

Fig. 6. (a) (C) TEM-BF micrograph of an Al-Zr-rich region in the interdendritic zone (region marked as "Fig. 6a" in the IPFZ in Fig. 4b). (b) (C) TEM-DF micrograph marked with white rectangle in (a). (c) SADP from the region marked in green in (a). Inset on bottom right shows the indexed simulated diffraction pattern. For details see text. (For interpretation of the references to color in this figure legend, the reader is referred to the web version of this article.)

such as those in Fig. 5. Most of the SADP (Fig. 6c) can be indexed (cf. inset simulated diffraction pattern on bottom right) as either Al_3Zr_5 or Al_4Zr_5, both along the zone axis [1 $\bar{1}$ 00]. Both Al-Zr-rich phases are hexagonal, having the $P6_3/mcm$ space group (Al_3Zr_5: ICDD- 04–003-0819, Al_4Zr_5: ICDD −00–048-1382). More details about the hexagonal phase will be discussed in Section 4. The CTEM-DF image (Fig. 6b) shows two types of contrast. One is very bright which comes from the reflection ($\bar{1}\ \bar{1}$ 20) in the diffraction pattern, around which the contrast aperture was placed, to which discrete nano-sized regions can be associated. The second contrast is weaker and covers the region that also appears bright in Fig. 6a. This contrast may be associated to the diffused ring of which center of mass coincides with $\{\bar{1}\ \bar{1}\ 21\}$ in Fig. 6c, typical for amorphous material. This reflection is also the strongest for powder diffraction patterns of either Al-Zr-rich candidates. For the estimation of the volume fraction in the AC alloy, SEM-BSE images were used for the Al-Zr-rich phase in the grain boundaries and STEM-DF images for the A2 and B2 phases. The volume fraction was estimated to be (8 ± 4)% for the hexagonal Al-Zr-rich phase, (36 ± 4)% for the B2 phase, and the rest for the A2 phase.

3.1.2. Annealed state (AN)

After annealing, the dendritic structure cannot be discerned anymore and the equiaxed grains become clearer (Fig. 7a), forming grain and subgrain boundaries. The average grain size is 78 ± 10 µm. Large second phase precipitates (black core surrounded by bright rim) are found at the grain boundaries (blue arrows in Fig. 7a-b). Also, the subgrain boundaries are found to be replaced with a black-bright dual phase that is also a common feature within the large grains (red arrows in Fig. 7b-c). These interfacial layers can be as thick as 1 µm. Fig. 7d show the structure inside the equiaxed grains at a high magnification, which also reveals a now continuous black phase that surrounds bright precipitates. The large second phase precipitates at the grain boundaries are rich in Al and Zr (see Fig. A1- Appendix A of supplementary data), whereas the bright interfacial layer surrounding the Al-Zr particles is rich in Nb, Mo and Ta. This elemental partitioning also applies to the dual phase structure found at subgrain boundaries at a higher magnification (Fig. 7c), as revealed by qualitative EDX points of these regions, i.e., a dark phase rich in Al and Zr, and a bright phase rich in Nb, Mo and Ta (cf. Table 2).

To identify the phases mentioned above, X-ray diffraction (XRD) patterns were indexed as shown in Fig. 8. Three phases, (B2, A2 and hexagonal intermetallic phase) are identified by comparing their patterns based on PowderCell simulations for both states. The A2 and B2 match well with the pattern acquired for the AC alloy (Fig. 8a), with corresponding lattice parameters a_1 = 3.28 Å and a_2 = 3.32 Å. The lattice parameters of the A2 and B2 phases in the AN alloy are determined as a_3 = 3.27 Å and a_4 = 3.31 Å, respectively (Fig. 8b). Based on previous results of an alloy of similar composition [10,17], the peaks that do not match with neither the A2 nor the B2 phase, are indexed as the hexagonal intermetallic phase (space group: $P6_3/mcm$).

The EDX-coupled EBSD system indexes the large equiaxed grains in the AN as "BCC" (rich in Nb, Ti and Zr), even though it has a dual A2/B2 nanostructure (see separate peaks in Fig. 8b), and the precipitates located at the grain boundaries are indexed as a hexagonal crystal structure (space group: $P6_3/mcm$) with a composition rich in Al and Zr. (cf. Fig. A2- Appendix A of supplementary data), corroborating the results obtained by XRD and by Jensen et al. [26]. TEM results demonstrate a heterogeneous nanostructure that consists of precipitates with B2 phase (plate-like with thickness ≈ 10 – 100 nm) embedded in a continuous phase (chan-

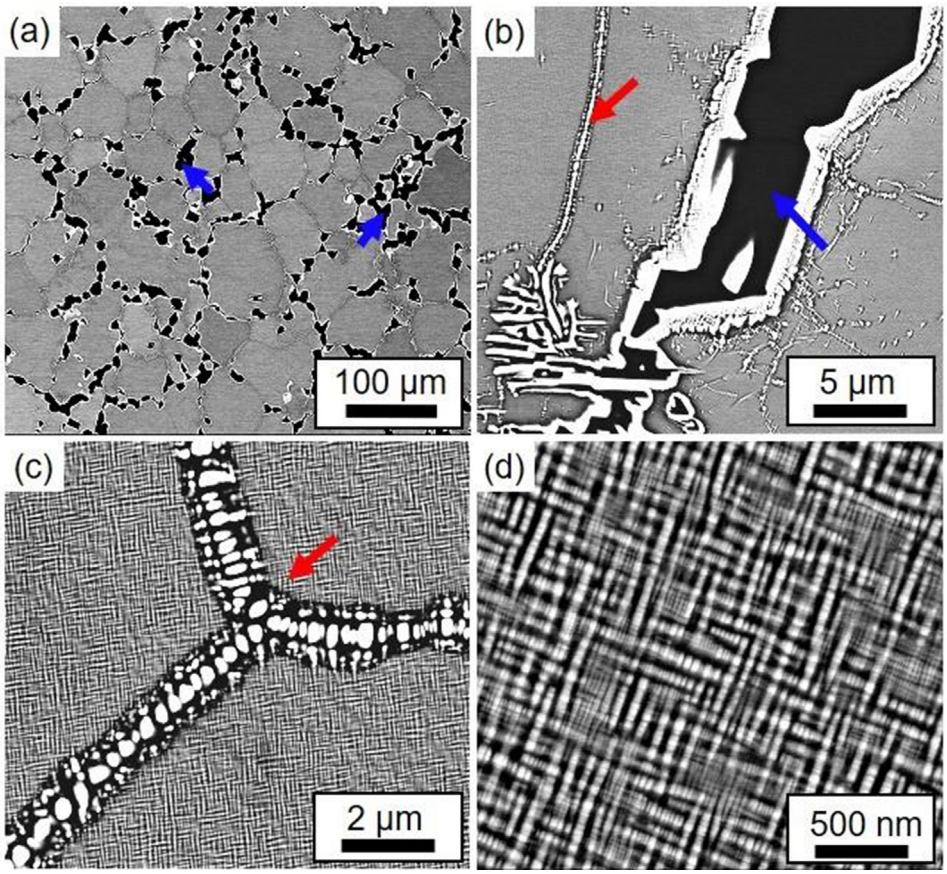

Fig. 7. SEM-BSE micrographs of the AN alloy, revealing features at different length scales. (a) Low magnification image showing an equiaxed microstructure with large secondary precipitates at grain boundaries. (b) Detail of coarsened precipitate at grain boundaries. (c) Detail of two-phase replacing the subgrain grain boundaries (d) High magnification image showing a nanometric two-phase basket-weave lamellar structure within grains. Blue and red arrows respectively mark coarse grain boundary precipitates and finer subgrain boundary precipitates. (For interpretation of the references to color in this figure legend, the reader is referred to the web version of this article.)

nels with thickness ≈ 3 – 30 nm). For a detailed description of the TEM analysis see Fig. A3 of supplementary data.

These results show that the microstructure in the annealed state with the condition in the present work (1400 °C for 24 h and cooled at ≤ 4 K/min) reproduces the microstructure reported with the conditions in the literature (1400 °C for 24 h + hot isostatic pressing at 1400 °C for 4 h and 205 MPa, cooled at 10 K/min) [8,10].

Table 2 summarizes the chemical composition of the phases in the different regions for the AC and AN alloy. For the estimation of the volume fraction in the AN alloy, SEM-BSE images were used for the Al-Zr-rich phase in the grain boundaries and STEM-DF images for the A2 and B2 phases. The volume fraction was estimated to be (13 ± 6)% for the hexagonal Al-Zr-rich phase, (34 ± 8)% for the B2 phase, and the rest for the A2 phase.

3.2. Differential thermal analysis (DTA)

Fig. 9 shows that two peaks are distinguished at the following temperature ranges: the first peak is detected between ≈ 820 °C and 1543 °C, which has an exothermic character; the second and smallest peak, with an endothermic character, is detected between 1555 °C and 1613 °C. The final 7 °C of the curve show a steep path towards the maximum temperature of the analysis shown by the dashed line at the end of the last peak (which coincides with the maximum temperature of the equipment), and it therefore could extend to higher temperatures.

3.3. Thermodynamic calculations

3.3.1. Scheil simulation for non-equilibrium

In Fig. 10, the fraction of the dependences of the solid phases on the temperature during solidification is shown for the studied RSA based on the experimentally measured composition in Table 1.The temperatures of start, $T_{L,Scheil}$ (solid < 0.01%), and completion, $T_{S,Scheil}$, of Scheil modeling and the temperatures of start, $T_{L,Eq.}$, and completion, $T_{S,Eq.}$, of equilibrium are given in Table 3, as calculated using the TCNI10 and TCHEA3 database.

Fig. 10 represents the Scheil solidification diagram using the TCHEA3 database, which shows the formation of a single disordered A2 phase (BCC_B2#1) that is rich in Al, Ti and Zr. Solidification starts at $T_{L,Scheil}$ = 1895 °C and ends at $T_{S,Scheil}$ = 1345 °C with a solidification range of $\Delta T_{s,\ Scheil}$ = 550 °C. When BCC_B2#1 reaches a fraction of solid ≈ 0.72, the SIGMA phase starts solidifying between 1475 °C and 1360 °C. At this temperature, the intermetallic phase Al4Zr5 appears with approx. X = 0.85 until almost the end of the solidification, where the C14_LAVES phase then appears. The Scheil-Gulliver model diagram was also calculated for the TCNI10 database (see Fig. B1-Appendix B of supplementary data), and it shows the same results as the TCHEA3 database.

3.3.2. Equilibrium

The property diagrams of the RSA alloy with the chemical composition given in Table 1 were calculated using CALPHAD analysis. The property diagram describes the relative amount of the phases in equilibrium as a function of their evolution with temperature,

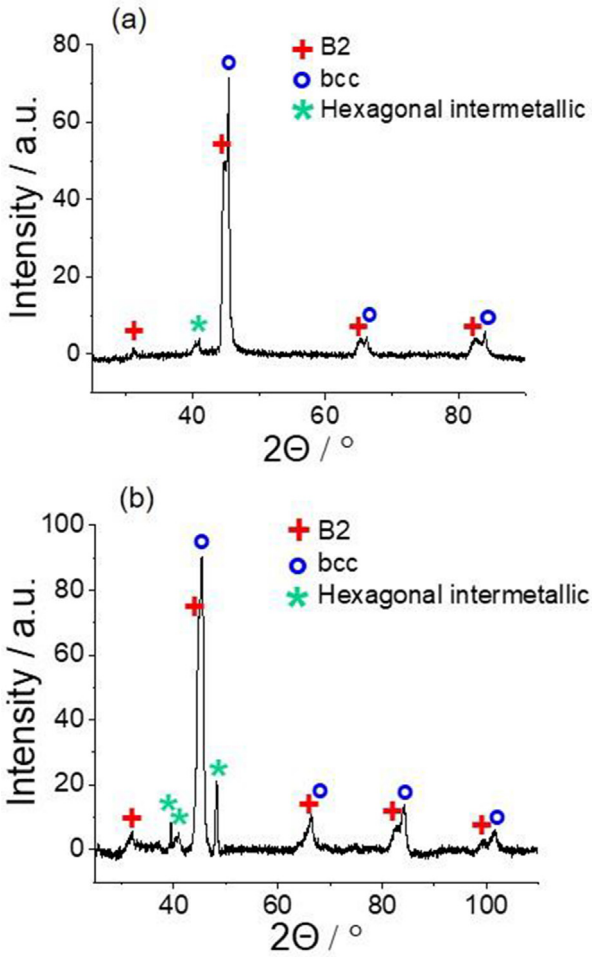

Fig. 8. XRD pattern (a) AC state (b) AN state.

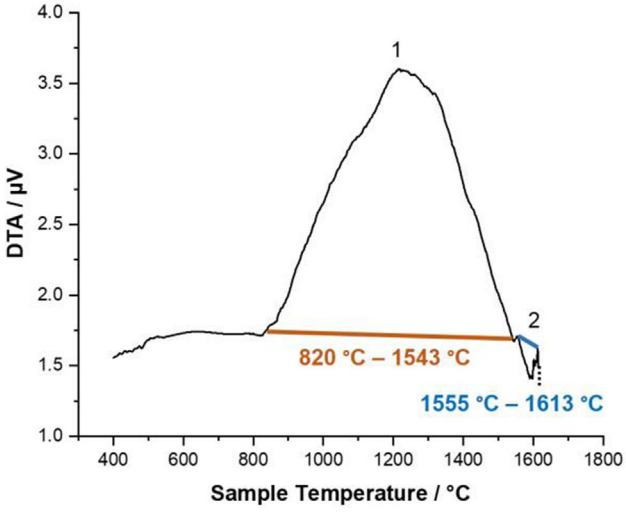

Fig. 9. DTA signal of the AN specimen as a function of the temperature recorded during the heating ramp up to 1620 °C. The signal is corrected by a blank measurement.

assuming the transformation rate is extremely slow or that species diffuse at a very fast rate [27]. The calculated equilibrium phases and their volume fractions in the temperature range from 600 °C to 2000 °C are shown in Fig. 11 for the TCHEA3 database. A detailed

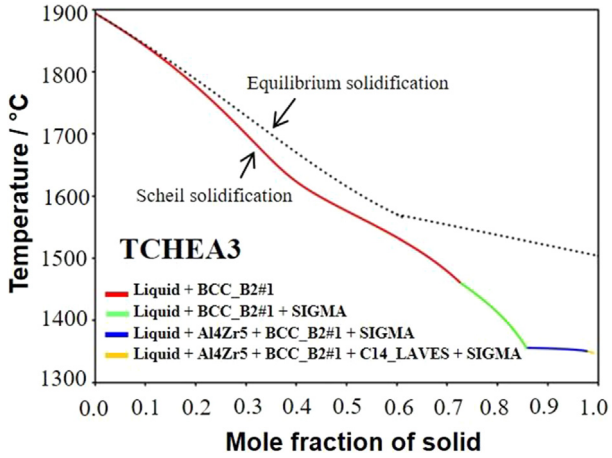

Fig. 10. Scheil solidification diagram for the RSA using the ThermoCalc software with database TCHEA3 database (cf. Fig. B1-Appendix B of supplementary data for database TCNI10).

Table 3
Liquidus and solidus temperature for Scheil and equilibrium solidification in both databases.

Database	T_L (Scheil-Eq.) / °C	T_S (Scheil) / °C	T_S (Eq.) / °C
TCHEA3	1895	1345	1503
TCNI10	1895	1345	1503

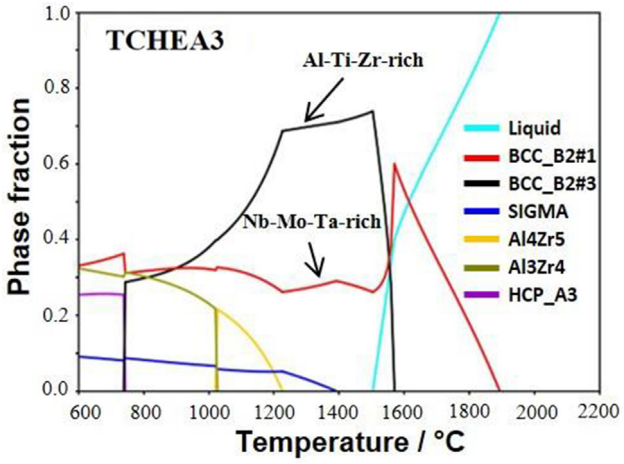

Fig. 11. Property diagram for the RSA using ThermoCalc software (TCHEA3 database). (cf. Fig. B2 and Table B2-Appendix B of supplementary data for database TCNI10).

description of the equilibrium phase transformation temperatures (in °C) in the studied alloy is given in Table B1 and Table B2 (Appendix B of supplementary data) for TCHEA3 and TCNI10, respectively. In Fig. 11 the beginning of solidification is marked by the formation of a single bcc phase at 1895 °C (Table B1-Appendix B of supplementary data), which is rich in Nb, Mo and Ta (BCC_B2#1), until another bcc phase named BCC_B2#3 and rich in Al, Ti and Zr starts appearing at 1570 °C. The formation of SIGMA at T = 1388 °C is also indicated with a low final fraction of the phase (<10%). At 1225 °C, a phase rich in Al and Zr appears, i.e., Al4Zr5, and at 1025 °C this phase seems to transform into Al3Zr4, which continues forming below 600 °C. Lastly, at 743 °C the formation of HCP_A3 is anticipated, which is mostly rich in Ti. The results obtained for the TCNI10 database are the same for the TCHEA3 database (see Fig. B2 and Table B2-Appendix B).

Fig. 12 represents a comparison of the mole fraction of the elements in the equilibrium bcc phases calculated at 1000 °C with the TCHEA3 database (cf. Table B4-Appendix B of supplementary data for the TCNI10 database). At 1000 °C, the two databases show the presence of two bcc phases in equilibrium and in both cases, these are one Al-Ti-Zr-rich and one Mo-Nb-Ta-rich phase. The phase composition indicates that the first phase to solidify is rich in Nb, Mo and Ta while the second one is rich in Al, Ti and Zr (cf. Fig. 11). In addition, the temperature where the first and second phase appear is similar for both databases (cf. Table B1 and Table B2-Appendix B of supplementary data). The HCP_A3 phase, rich in Al, Ti and Zr (cf. Table B7 and Table B8-Appendix B of supplementary data), is anticipated to form at lower temperatures. TCNI10 and TCHEA3 indicate the formation of the phase SIGMA at the same temperature with a very small amount (<10%). Both databases indicate the formation of Al-Zr-rich phases (Al4Zr5 and Al3Zr4).

Fig. 13a represents a simulation assuming that the bcc phases are the only solid phases that are formed, in order to identify the miscibility gap and the difference in composition and volume fraction of the bcc phases. Here, the mole fraction of Al is plotted against temperature, indicating how the formation of the bcc phases varies with varying Al and Zr content, while the composition of the rest of the elements remains fixed (at X_{Mo} = 0.1019, X_{Nb} = 0.2023, X_{Ta} = 0.0676, X_{Ti} = 0.2079). The color-coded legend inset in Fig. 13a denotes the boundaries at which a phase transformation exists. The incomplete light blue line (BCC_B2#3) is due to a lack of information on that special projection. The marked region of dashed gray lines in the graph (Fig. 13a) is made as an attempt to show where the miscibility gap region closes. However, the exact composition at which the miscibility gap closes is not known since the diagram is a projection. Considering the experimentally determined mole fraction of Al in the alloy (X_{Al} = 0.2103), the equilibrium conditions were calculated at 2000, 1700, 1520 and 1200 °C (red vertical line in Fig. 13a), as shown in Fig. 13b (calculated phase fractions and composition of the phases are summarized in Table B9-Appendix B of supplementary data). At 2000 °C, only the liquid is present whereas at 1700 °C the first bcc phase (BCC_B2#1) already appears. At this temperature, the volume fraction of BCC_B2#1 (rich in Nb, Mo, and Ta) is 0.32 and the rest is liquid. At 1520 °C, the BCC_B2#1 (Nb-Mo-Ta-rich), BCC_B2#3 (Al-Ti-Zr-rich) and liquid are in equilibrium with mole fractions of 0.26, 0.64 and 0.10, respectively. Finally, at 1200 °C, only BCC_B2#1 and BCC_B2#3 will be in equilibrium with mole fractions of 0.30 and 0.70, respectively.

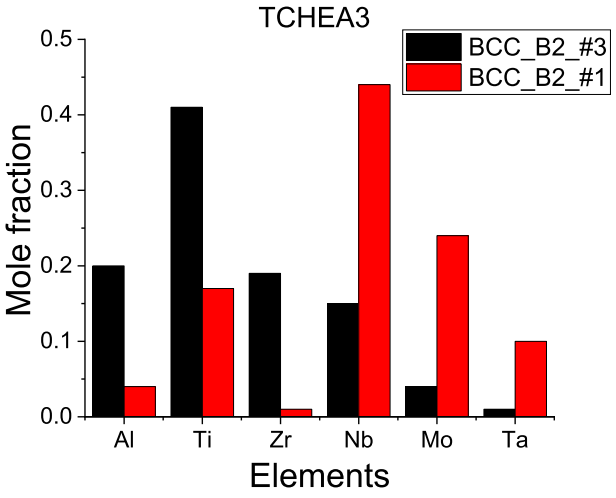

Fig. 12. Mole fraction of the elements in equilibrium phases for the studied alloy at T = 1000 °C (1273 K) as calculated with the TCHEA3 database (cf. Table B4-Appendix B of supplementary data for the TCNI10 database).

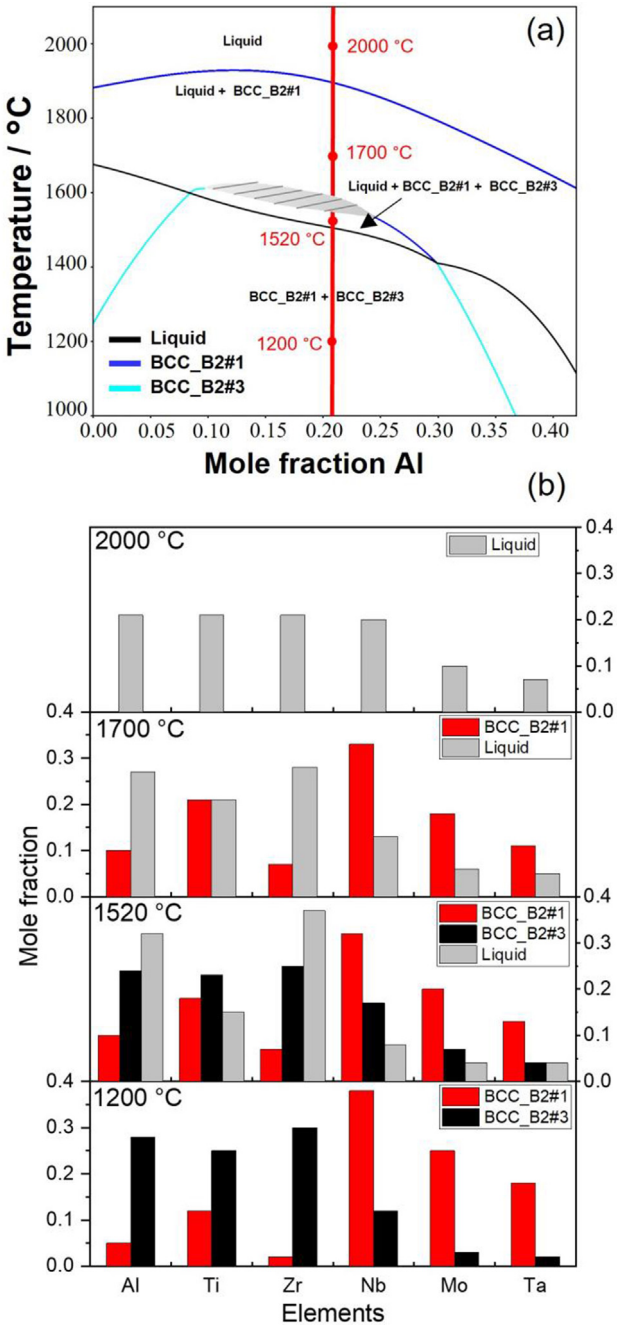

Fig. 13. (a) Mole fraction of Al vs temperature in equilibrium considering only the formation of bcc phases and liquid, using the TCHEA3 database. A miscibility gap region that closes in the region marked with dashed gray lines is shown. (b) Mole fractions of the elements of equilibrium phases in the studied alloy, considering only the formation of bcc phases at 2000, 1700, 1520 and 1200 °C respectively, calculated with the TCHEA3 database.

4. Discussion

The microstructural analysis demonstrates that the $AlMo_{0.5}NbTa_{0.5}TiZr$ RSA in AC condition presents dendritic and interdendritic zones with differences in composition and a mixture of A2/B2 phases ≈ 2 – 20 nm, and the presence of a residual eutectic rich in Al and Zr inside the interdendritic region (Fig. 2c). The diffuse

ring and the presence of bright areas in Fig. 6b reveal that the Al-Zr-rich phase region in the AC is formed by crystalline as well as amorphous portions, the latter being larger, with a 95 ± 4% of area fraction. Thus, at this cooling rate and probably due to the strong solute segregation to the interdendritic region, the conditions for forming an amorphous phase are fulfilled. In fact, Zr-Al alloys are well-known for their glass-forming ability [28,29], which is even further pronounced in the presence of the other elements. On the other hand, the AN state shows the presence of larger (≈ 10 – 100 nm) A2/B2 phases than in the AC state, and an increment of ≈ 5% in the volume fraction of the Al-Zr-rich phase (hexagonal $P6_3/mcm$), which can be due to its full crystallization. A good agreement with what was reported by Senkov et al. [8] and Jensen et al. [10,26] for the fully heat-treated state is thus found, with the results shown here for only annealing at 1400 °C (without hot isostatic pressing treatment at the same temperature for further 4 h).

The AC results obtained experimentally may be primarily simulated by the Scheil model, which assumes total diffusion in the liquid and no diffusion in the solid. In the Scheil solidification model, both databases evaluated here show that even at 1400 °C, complete solidification is not reached. The Scheil model indicates the formation of a single Al-Ti-Zr-rich bcc (A2) phase until the fraction of solid reaches ≈ 72% (Fig. 10). However, a separation of the two bcc phases should be visible when comparing with the experimental AC state. Therefore, additional calculations using the uncommon miscibility gap option were performed, still showing the formation of a single A2 phase.

On the other hand, the formation of the intermetallic Al_4Zr_5 phase is indicated in the Scheil solidification. Unlike the calculations, the hexagonal phase in the experimental results does not show an Al_4Zr_5 stoichiometry. In fact, the average pattern quality shown in Fig. 4b for these regions is poor yet still indexable: considering the experimental conditions in the present work, the manual indexation of individual high quality Kikuchi patterns (not shown here) suggests evidence of an unknown stoichiometry (Al_x-Zr_y) for a phase with hexagonal symmetry but that is not identified as hexagonal solid solution (HCP), the latter being reported elsewhere [9]. Evaluating the differences between the lattice cells of the two possible experimental ordered hexagonal phases (Al_3Zr_5 and Al_4Zr_5) shows that the surplus of Al atoms found in the Al_4Zr_5 phase is distributed along the c axis on the corners of the hexagon, only causing a slight repositioning of the remaining atoms in the cell when compared to Al_3Zr_5 (see Fig. C1-Appendix C of supplementary data). Although the distribution of the atoms is different, both phases belong to the same space group ($P6_3/mcm$). However, a detailed identification of this phase is beyond the scope of this publication and will follow in a separate contribution. Since the diffraction patterns between Al_3Zr_5 and Al_4Zr_5 resemble each other and considering that probably the Al_xZr_y phase of the present alloy probably is an intermediate phase between those two ($Al_{4-x}Zr_5$, $0 \leq x \leq 1$), the diffraction pattern shown in the Fig. 6c was indexed as the Al_4Zr_5 phase.

To understand the solidification path of the alloy, the Scheil model was implemented using the TCHEA3 database to calculate the mole fraction of solid vs the mole fraction of each element in the liquid (Fig. 14). This simulation evidences that there is a high segregation in the last liquid (85% of solid formation), rich in Al and Zr, regarding the original alloy composition. The calculated ratio X_{Zr} / X_{Al} at 85% of solid formation (Table 4) matches the experimental ratio X_{Zr} / X_{Al} of the Al-Zr-rich phase (Table 2), which is also close to the stoichiometry of the Al_4Zr_5 phase. This phase is stable almost at the end of solidification according to the calculations, and the Al-Zr-rich intermetallic phase is found in the interdendritic zone, which is also the last region that solidifies, showing a good agreement between the calculations and the experimental findings.

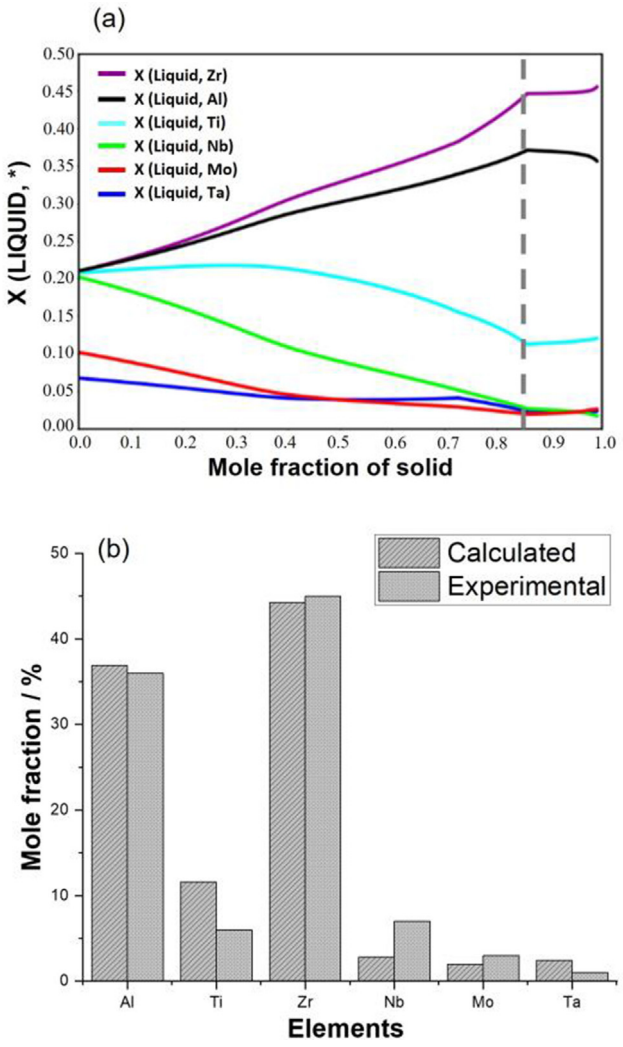

Fig. 14. (a) Mole fraction of solid vs mole fraction of each element in the liquid using Scheil model with the TCHEA3 database. X (Liquid, *) = mole fraction of element "*" in the liquid. (b) Comparison between calculated liquid composition at 0.85 mol fraction (85%) of the solid (dashed line in (a) and Table 4) and experimental composition of the Al-Zr-rich phase in the interdendritic region in AC (Table 2).

On the other hand, the microstructure of the AN alloy emerged after high temperature annealing at 1400 °C followed by furnace cooling and, as such, even only after 24 h, it is believed to be indicative of the stable high temperature phases. Therefore, the experimental results of the AN alloy are compared with the equilibrium calculations. In equilibrium, both databases (TCNI10 and TCHEA3) show the formation of two disordered bcc phases, one that is rich in Al, Zr and Ti, and another, rich in Nb, Mo and Ta. Furthermore, in the binary diagrams as well as in the ternaries calculated within the databases under study (not shown here), there is no modeling for a B2 (ordered) phases, so it is to be expected that the A2 (disordered) phase is the default phase. Thus, considering that the databases used in this paper do not distinguish between order and disorder, and based on the experimental phase composition of the bcc phases, it could be assumed that the calculated Al-Zr-Ti-rich phase is the B2, and the Nb-Mo-Ta-rich phase is the A2 obtained experimentally. In fact, the databases only indicate the presence of these two bcc phases (named BCC_B2#1 and BCC_B2#3) at that temperature (1400 °C) and, in both databases, solidification starts with the formation of the BCC_B2#1 (rich in higher melting Mo, Nb and Ta).

Table 4
Calculated composition of the last 15% of the liquid phase according to the Scheil solidification as shown in Fig. 14.

Database	Phase	Sol. mole fraction X_{sol}	Al	Mo	Nb	Ta	Ti	Zr	X_{Zr}/X_{Al}
TCHEA3	liquid	0.85	36.90	1.99	2.82	2.43	11.60	44.26	1.2

Experimental results show the presence of a dual phase structure composed of A2 and B2 phase in the AN alloy with channels and precipitates as in the AC alloy, but with smaller sizes for the latter. Jensen et. al [26], proposed that the precipitation of these phases may occur by spinodal decomposition during cooling, due to the compositional fluctuations in high temperature phases. Kadirval et al. [30] analyzed the details of a possible phase transformation pathway for this alloy, including a congruent spinodal decomposition upon heat treatment. The Fig. 13 confirms that a miscibility gap already exists at 1400 °C at the exact composition of the original alloy, where the two bcc phases coexist and the constituents are not completely miscible, pinpointing the possibility of a spinodal decomposition as suggested in the previous works [26,30] and the experimental results found in the present work. Moreover, the dual phase structure being present at compositions found in the interdendritic region of the AC alloy and the dendritic regions of the AN alloy is also in line with the wide miscibility gap found Fig. 13a, where both phases are indicated to coexist.

Although experimental evidence of SIGMA is neither shown in the AC state nor in the AN state, under equilibrium conditions, the stability of this phase has been studied on several occasions for both conventional and multicomponent alloys [35–38] where both temperature and annealing time play an important role, and there is evidence that longer annealing times (>500 h) are required to stabilize this phase. Therefore, SIGMA may be thermodynamically stable but still not developed after 24 h of annealing. The other phases proposed to be formed in equilibrium conditions (Al_3Zr_4 and HCP_A3), are stable at temperatures below the annealing temperature, so they are not expected to appear in the experimental results.

The Scheil diagram, Fig. 10, indicates that, due to the strong solute segregation, the last drop of liquid may solidify at a temperature as low as 1345 °C, about 50 °C below the annealing temperature (1400 °C) and 150 °C lower than the equilibrium solidus temperature (1503 °C). This means that the local melting temperature at the grain boundaries and subgrain boundaries can be relatively low. Together with the assistance from additional interfacial energies released, these can result in the formation of liquid-like interfacial phases during the annealing at 1400 °C, as observed in several ceramics [31–34]. The formation of such liquid-like phases dramatically enhances the diffusion of solute atoms at the interfacial regions. This can then explain the coarsened microstructure at the grain and subgrain boundaries, especially the formation of large secondary Al-Zr-rich precipitates with the continuous surrounding layer around them (c.f. Fig. 7 for the details) in the AN sample. The formation of interfacial phases at both grain and subgrain boundaries has important consequences for the mechanical performance of the RSA, the detailed study of which will be presented elsewhere.

Senkov et al. [16] studied the $AlMo_{0.5}NbTa_{0.5}TiZr$ alloy using the Pandat Ti database to model Scheil solidification. They found that solidification starts with the formation of a bcc phase (enriched with Mo, Nb and Ta), and that a very small amount (≈ 0.3%) of the intermetallic phase Al_2Zr_3 forms at the end of solidification. Furthermore, they showed the formation of three phases at equilibrium: "bcc1", Ti_3Al and Al_2Zr_3. Furthermore, Whitfield et al. [17] anticipated the formation of two bcc phases at high temperature using the SSol5 database, whereas Al_4Zr_5 formed close to 1000 °C, and a B2 and HCP phase formed below 1000 °C (in equilibrium conditions) in their calculations. The latter resembles the results obtained in the calculations from the present work. Unfortunately, the composition of each phase was not reported by Whitfield et al., which makes a comparison with the results presented here impossible. However, later analyses by XRD and TEM have demonstrated that the "B2" phase described by the SSol5 database is in fact a disordered A2 phase [39]. Thus, it must be considered that the databases usually do not make a distinction between order and disorder, which leads to a decline of accuracy in the calculations.

Finally, from the differential thermal analysis shown in Fig. 9, the observed peaks can be related to the phase transformations according to the experimental observation, and these phase transformations can be compared with the thermodynamic calculations presented in Fig. 11 (equilibrium conditions). The first peak can be associated with solid–solid phase transformations and the second peak with a melting process (Fig. 9). Although exact equilibrium conditions cannot be achieved during DTA, the results are obtained in conditions close to equilibrium because a slow heating rate of 5 K/min was used and therefore, these results may be used to verify the thermodynamic calculations. The widest peak, observed between 820 °C and 1543 °C, is likely to be composed of several overlaying peaks. These could be related to the increase of amount and final dissolution of the major phase BCC_B2, enriched in Al, Zr and Ti (BCC_B2#3 according to both databases) as well as early stages of a premelting at grain boundaries. The last peak at a temperature above 1555 °C can be related to a first event of bulk melting, which can be clearly seen in the equilibrium calculations (Fig. 11). Note that even from the equilibrium calculations, the liquid and the two bcc phases (BCC_B2#1 and BCC_B2#3) coexist already at 1503 °C. Considering the broadness of the second peak, it is possible that an overlap of different peaks takes place, suggesting that liquification may start happening in parallel to dissolution of the BCC_B2 phase. These results indicate that, from the point of view of hot cracking, the alloy starts the formation of liquid at a temperature ≈ 200 °C higher than the temperature where liquid appears in single crystal (SX) Ni-based superalloys (1345 °C for the SX CMX4 alloy). However, grain boundary instabilities and lack of room temperature ductility were observed (not shown here), and therefore, mechanical properties at high temperature, as well as corrosion behavior should be assessed to stablish whether this alloy has potential for high temperature applications such as Ni-based superalloy.

5. Summary and conclusions

In the present work, an approach to study the phase stability and solidification behavior of the RSA $AlMo_{0.5}NbTa_{0.5}TiZr$ was implemented using CALPHAD calculations with two different databases (TCNI10 and TCHEA3), and compared with experimental data from as-cast, AC, and annealed state, AN (AC + 1400 °C for 24 h). The as-cast state was compared with Scheil, whereas the annealed state was compared with equilibrium calculations. The following conclusions can be drawn from the results:

- The as-cast state shows a dendritic structure with a A2/B2 phase structure in both the dendritic and interdendritic regions, which are an order of magnitude smaller than the A2/B2 phase structure reported previously and reproduced in the present

work. Annealing at 1400 °C for 24 h crystallizes completely a mostly amorphous phase that is rich in Al and Zr within the interdendritic region in the as-cast state.

- Thermodynamic calculations using the Scheil-Gulliver model indicated the formation of a single bcc phase in both databases, although the presence of both A2 and B2 was experimentally demonstrated for the as-cast state. Phases such as SIGMA and LAVES also appear in the Scheil calculations even though no evidence is found in the experimental data for the conditions evaluated here. However, both databases anticipated the formation of the Al_4Zr_5 intermetallic phase, which has the space group of the Al-Zr-rich intermetallic found experimentally ($Al_{4-x}Zr_5$, $0 \leq x \leq 1$), thus showing a partial agreement with the experimental data.
- Equilibrium thermodynamic calculations show the formation of two bcc phases, i.e., one rich in Al, Zr and Ti and a second one, rich in Mo, Nb and Ta, which is supported by the present and previous experimental results, although the calculations do not reflect the differences between ordered and disordered phases. The possibility of a spinodal decomposition resulting in the patterned microstructure observed experimentally was confirmed through the miscibility gap calculations.
- DTA results proved that in this alloy the liquid phase appears at a temperature higher than for Ni-base alloys, which could make it attractive for high temperature applications. However, other properties of this material, such as tensile behavior and corrosion resistance, need to be evaluated when pondering this RSA for structural applications. In particular, the role and mechanisms of interfacial phase changes during annealing need to be explored. Further efforts are currently in progress with a focus on these aspects.
- Finally, both databases evaluated here reproduce the same results, showing that the TCNI10 database is as useful for this alloy as the TCHEA3 database. However, there are still many discrepancies between calculations and experimental results. Therefore, more research should be developed to improve the modeling, including B2 ordering, and more effort could be made by experimentalists to investigate important ternaries that could provide information for the model improvements.

CRediT authorship contribution statement

Patricia Suárez Ocaño: Experimental Methodology, CALPHAD Calculations TCNI10 and TCHEA3, Formal analysis, Data curation, Writing – original draft. **Suzana G. Fries:** CALPHAD Calculations TCNI10 database, Formal analysis, Writing – review & editing. **Inmaculada Lopez-Galilea:** DTA Analysis, Writing – review & editing. **Reza Darvishi Kamachali:** Funding acquisition, Writing – review & editing. **Janina Roik:** ICP-OES measurements. **Leonardo Agudo Jácome:** Conceptualization, Methodology, Formal analysis, Writing – original draft, Supervision, Funding acquisition.

Declaration of Competing Interest

The authors declare that they have no known competing financial interests or personal relationships that could have appeared to influence the work reported in this paper.

Acknowledgement

PSO and LAJ acknowledge funding by the Deutsche Forschungsgemeinschaft (DFG) within the Project n°. 398838389. ILG acknowledge funding by the Deutsche Forschungsgemeinschaft (DFG) in the framework of the collaborative research center SFB/TR 103 through project T4. All authors acknowledge Dipl.-Ing. Hans Chen, Dr. Alexander Kaufmann, Prof. Martin Heilmaier from Kalsruher Institut for Technology for the fabrication of the alloy. PSO and LAJ acknowledge Prof. Gert Nolze, Romeo Saliwan Neumann for the EBSD analysis, Hennig Goldbeck for XRD, René Hesse for the EDX maps, Carlos Abad for the ICP-OES measurements and Stefan Reinsch for the DTA measurements. PSO and SGF thank the use of the facilities of ZGH (Center for Interface-Dominated High-Performance Materials). All authors acknowledge Dr. Axel Kranzmann for the fruitful discussion, and Dr. Julian Rosalie for the support in the data process.

Supplementary data

Supplementary data to this article can be found online at https://doi.org/10.1016/j.matdes.2022.110593.

References

[1] A.P. Mouritz, Superalloys for gas turbine engines, Introduction to Aerospace Mater. (2012) 251–267, https://doi.org/10.1533/9780857095152.251.
[2] L. Liu, J. Zhang, C. Ai, Nickel-Based Superalloys, Encyclopedia Mater.: Metals Allloys 1 (2022) 294–304, https://doi.org/10.1016/B978-0-12-803581-8.12093-4.
[3] F. Zhang, C. Wang, Y. Wu, L. Zhou, Q. Tian, Microstructural stability and mechanical properties of GH742 Ni-based wrought superalloy for turbine disk applications, Mater. Sci. Eng., A 832 (2022) 142488, https://doi.org/10.1016/j.msea.2021.142488.
[4] R.C. Reed, The Superalloys: Fundamentals and Applications Cambridge University Press, 2006: p. 372pp. https://doi.org/10.1017/S0001924000087509.
[5] M. Wang et al., Designing VxNbMoTa refractory high-entropy alloys with improved properties for high-temperature applications, Scr. Mater. 191 (2021) 131–136, https://doi.org/10.1016/j.scriptamat.2020.09.027.
[6] W. Wei, T. Wang, C. Wang, M. Wu, Y. Nie, J. Peng, Ductile W0.4MoNbxTaTi refractory high-entropy alloys with excellent elevated temperature strength, Mater. Lett. 295 (2021) 129753, https://doi.org/10.1016/j.matlet.2021.129753.
[7] Y.D. Wu, Y.H. Cai, X.H. Chen, T. Wang, J.J. Si, L. Wang, Y.D. Wang, X.D. Hui, Phase composition and solid solution strengthening effect in TiZrNbMoV high-entropy alloys, Mater. Des. 83 (2015) 651–660, https://doi.org/10.1016/j.matdes.2015.06.072.
[8] O. Senkov, D. Isheim, D. Seidman, A. Pilchak, Development of a refractory high entropy superalloy, Entropy 18 (3) (2016) 102, https://doi.org/10.3390/e18030102.
[9] O.N. Senkov, J.K. Jensen, A.L. Pilchak, D.B. Miracle, H.L. Fraser, Compositional variation effects on the microstructure and properties of a refractory high-entropy superalloy AlMo0.5NbTa0.5TiZr, Mater. Des. 139 (2018) 498–511, https://doi.org/10.1016/j.matdes.2017.11.033.
[10] J.K. Jensen, B.A. Welk, R.E.A. Williams, J.M. Sosa, D.E. Huber, O.N. Senkov, G.B. Viswanathan, H.L. Fraser, Characterization of the microstructure of the compositionally complex alloy $Al_1Mo_{0.5}Nb_1Ta_{0.5}Ti_1Zr_1$, Scr. Mater. 121 (2016) 1–4, https://doi.org/10.1016/j.scriptamat.2016.04.017.
[11] D.B. Miracle, M.-H. Tsai, O.N. Senkov, V. Soni, R. Banerjee, Refractory high entropy superalloys (RSAs), Scr. Mater. 187 (2020) 445–452, https://doi.org/10.1016/j.scriptamat.2020.06.048.
[12] H.L. Chen, H.H. Mao, Q. Chen, Database development and Calphad calculations for high entropy alloys: Challenges, strategies, and tips, Mater. Chem. Phys. 210 (2018) 279–290, https://doi.org/10.1016/j.matchemphys.2017.07.082.
[13] O.N. Senkov, C. Zhang, A.L. Pilchak, E.J. Payton, C. Woodward, F. Zhang, CALPHAD-aided development of quaternary multi-principal element refractory alloys based on NbTiZr, J. Alloy. Compd. 783 (2019) 729–742, https://doi.org/10.1016/j.jallcom.2018.12.325.
[14] S. Gorsse, O.N. Senkov, About the Reliability of CALPHAD Predictions in Multicomponent Systems, Entropy 20 (12) (2018) 899, https://doi.org/10.3390/e20120899.
[15] A.F. Andreoli, R.G. Mendes, V.T. Witusiewicz, O. Shuleshova, M.A. van Huis, K. Nielsch, I. Kaban, Phase constitution and microstructure of the NbTiVZr refractory high-entropy alloy solidified upon different processing, Acta Mater. 221 (2021) 117416, https://doi.org/10.1016/j.actamat.2021.117416.
[16] O.N. Senkov, S.V. Senkova, C. Woodward, Effect of aluminum on the microstructure and properties of two refractory high-entropy alloys, Acta Mater. 68 (2014) 214–228, https://doi.org/10.1016/j.actamat.2014.01.029.
[17] T.E. Whitfield, H.J. Stone, C.N. Jones, N.G. Jones, Microstructural Degradation of the $AlMo_{0.5}NbTa_{0.5}TiZr$ Refractory Metal High-Entropy Superalloy at Elevated Temperatures, Entropy 23 (1) (2021) 80, https://doi.org/10.3390/e23010080.
[18] D.B. Miracle, O.N. Senkov, A critical review of high entropy alloys and related concepts, Acta Mater. 122 (2017) 448–511, https://doi.org/10.1016/j.actamat.2016.08.081.

[19] J.O. Andersson et al., Thermo-Calc & DICTRA, computational tools for materials science, Calphad 26 (2) (2002) 273–312, https://doi.org/10.1016/S0364-5916(02)00037-8.
[20] W. Kraus, G. Nolze, POWDER CELL - a program for the representation and manipulation of crystal structures and calculation of the resulting X-ray powder patterns, J. Appl. Cryst. 29 (3) (1996) 301–303, https://doi.org/10.1107/S0021889895014920.
[21] *Standard Test Methods for Determining Average Grain Size.* ASTM Designation: E112 − 13, 2013.
[22] P.A. Stadelmann, EMS - a software package for electron diffraction analysis and HREM image simulation in materials science, Ultramicroscopy 21 (2) (1987) 131–145, https://doi.org/10.1016/0304-3991(87)90080-5.
[23] C.A. Schneider, W.S. Rasband, K.W. Eliceiri, NIH Image to ImageJ: 25 years of image analysis, Nat. Methods 9 (7) (2012) 671–675, https://doi.org/10.1038/nmeth.2089.
[24] H.L. Lukas, S.G. Fries, B. Sundman, COMPUTATIONAL THERMODYNAMICS The Calphad Method. (2010), https://doi.org/10.1017/CBO9780511804137.
[25] D. Pelton, A., Equilibrium and Scheil-Gulliver Solidification, Phase Diagrams and Thermodynamic Modeling of Solutions 8 (2019) 133–148, https://doi.org/10.1016/B978-0-12-801494-3.00008-7.
[26] J.K. Jensen, Characterization of a High Strength, Refractory High Entropy Alloy, AlMo0.5NbTa0.5TiZr, PhD Dissertation. The Ohio State University, 2017: p. 1–227. http://rave.ohiolink.edu/etdc/view?acc_num=osu1492175560975813.
[27] N. Saunders, A.P. Miodownik, CALPHAD Calculation of Phase Diagrams, Pergamon Materials Series 1 (1998) 299–408, https://doi.org/10.1016/S1470-1804(98)80030-8.
[28] T. Wang, Z. Jin, J.-C. Zhao, Thermodynamic assessment of the Al-Zr binary system, J. Phase Equilibria and Diffusion 22 (5) (2001) 544–551, https://doi.org/10.1007/s11669-001-0072-4.
[29] A. Takeuchi, A. Inoue, Classification of bulk metallic glasses by atomic size difference, heat of mixing and period of constituent elements and its application to characterization of the main alloying element, Mater. Trans. 46 (12) (2005) 2817–2829, https://doi.org/10.2320/matertrans.46.2817.
[30] K. Kadirvel, Z. Kloenne, J.K. Jensen, H. Fraser, Y. Wang, Phase-field modelling of transformation pathways and microstructural evolution in multi-principal element alloys, Appl. Phys. Lett. 119 (17) (2021) 171905, https://doi.org/10.1063/5.0065522.
[31] J. Luo, S.J. Dillon, M.P. Harmer, Interface Stabilized Nanoscale Quasi-Liquid Films, Microscopy Today 17 (4) (2009) 22–27, https://doi.org/10.1017/S1551929509001212.
[32] J. Luo, Stabilization of Nanoscale Quasi-Liquid Interfacial Films in Inorganic Materials: A Review and Critical Assessment, Crit. Rev. Solid State Mater. Sci. 32 (1–2) (2007) 67–109, https://doi.org/10.1080/10408430701364388.
[33] J. Luo, V.K. Gupta, D.H. Yoon, H.M. Meyer, Segregation-induced grain boundary premelting in nickel-doped tungsten, Appl. Phys. Lett. 87 (23) (2005) 231902, https://doi.org/10.1063/1.2138796.
[34] S.J. Dillon, M.P. Harmer, Multiple grain boundary transitions in ceramics: A case study of alumina, Acta Mater. 55 (15) (2007) 5247–5254, https://doi.org/10.1016/j.actamat.2007.04.051.
[35] G. Laplanche et al., Phase stability and kinetics of s-phase precipitation in CrMnFeCoNi high-entropy alloys, Acta Mater. 161 (2018) 338–351, https://doi.org/10.1016/j.actamat.2018.09.040.
[36] J. Wan, H. Ruan, J. Wang, S. Shi, The Kinetic diagram of sigma phase and its precipitation hardening effect on 15Cr-2Ni duplex stainless steel, Mater. Sci. Eng., A 711 (2018) 571–578, https://doi.org/10.1016/j.msea.2017.11.079.
[37] L.u. Zhang, L.i. Zhang, H. Wang, J. Li, J. Man, Z. Xu, J. Yu, G. Wan, W. Wang, B. Wu, Evolution of the microstructure and mechanical properties of an sigma-hardened high-entropy alloy at different annealing temperatures, Mater. Sci. Eng., A 831 (2022) 142140, https://doi.org/10.1016/j.msea.2021.142140.
[38] S. Antonov, J. Huo, Q. Feng, D. Isheim, D.N. Seidman, R.C. Helmink, E. Sun, S. Tin, σ and η Phase formation in advanced polycrystalline Ni-base superalloys, Mater. Sci. Eng., A 687 (2017) 232–240, https://doi.org/10.1016/j.msea.2017.01.064.
[39] M.J. Kriegel et al., High-temperature phase equilibria with the bcc-type ß (AlMo) phase in the binary Al-Mo system, Intermetallics 83 (2017) 29–37, https://doi.org/10.1016/j.intermet.2016.12.004.